Qeltite – the first terrestrial high-temperature mineral with a langasite-type structure from pyrometamorphic rock of the Hatrurim Complex

Irina O. Galuskina[1]*, Marcin Stachowisz[2], Yevgeny Vapnik[3], Grzegorz Zeliński[4], Krzysztof Woźniak[5], and Evgeny Galuskin[1]

[1]Institute of Earth Sciences, Faculty of Natural Sciences, University of Silesia, Będzińska 60, 41-205 Sosnowiec, Poland

[2] Institute of Geochemistry, Mineralogy and Petrology, University of Warsaw, Żwirki i Wigury 93, 02-089 Warsaw, Poland

[3]Department of Geological and Environmental Sciences, Ben-Gurion University of the Negev, POB 653, Beer-Sheva 84105, Israel

[4]Micro-Area Analysis Laboratory, Polish Geological Institute-National Research Institute, Rakowiecka 4, 00-975 Warsaw, Poland

[5]Department of Chemistry, University of Warsaw, Pasteura 1, 02-093 Warszawa, Poland

*Corresponding author e-mail address: irina.galuskina@us.edu.pl

Keywords: qeltite, new mineral, structure, Raman, langasite, pyrometamorphic rock, Hatrurim Complex

DOI: 10.1180/mgm.2024.38

Abstract: Qeltite (IMA2021-032), ideally $Ca_3Ti(Fe_2Si)Si_2O_{14}$, was found in gehlenite-rankinite-wollastonite paralava from a pyrometamorphic rock of the Hatrurim Complex at Nabi Musa locality, Judean Desert, West Bank, Palestine. It generally occurs as light-brown flattened crystals up to 40–50 μm in length and less than 5 μm in thickness. Its aggregates reach 100–200 μm in size. Its empirical crystal chemical formula based on 14 O is as follows: $(Ca_{2.96}Sr_{0.02}Mn_{0.01})_{\Sigma 2.99}Ti^{4+}(Fe^{3+}_{1.59}Si_{0.60}Al_{0.43}Ti^{4+}_{0.38}Cr_{0.01})_{\Sigma 3.02}(Si_{1.99}P_{0.01})_{\Sigma 2}O_{14}$. The strongest reflections in its calculated X-ray diffraction pattern are [*d*(Å), ***I***, *hkl*]: 3.12, ***100***, *111*; 2.85, ***61***, *201*; 2.85, ***48***, *021*; 2.32, ***45***, *211*; 6.93, ***31***, *100*; 1.81, ***30***, *212*. Qeltite is trigonal and it crystallizes in the noncentrosymmetric *P*321 space group, with $a = 8.0077(5)$ Å, $c = 4.9956(4)$ Å, $V = 277.42(4)$ Å^3 and $Z = 1$. Its microhardness VHN_{25} is 708(17) kg/mm^2, and its hardness on the Mohs scale is about 6. Its calculated density is 3.48 g/cm^3. It was found in fine-grained mineral aggregates within coarse-grained main minerals of rankinite-gehlenite paralava with subordinate wollastonite, Ti-bearing andradite and kalsilite. In these aggregates, the mineral is associated with khesinite, paqueite and pseudowollastonite, indicating a high-temperature genesis (about 1200°C). Its crystallization can be compared with the crystallization of minerals containing refractory inclusions in meteorites.

Introduction

In gehlenite paralava of the Hatrurim Complex, spreading across the territories of Israel and Palestine, a whole series of new minerals with langasite-type structure (Belokoneva *et al*., 1980; Mill *et al*., 1982; Kaminskii *et al*., 1983; Mill and Pisarevsky, 2000; Andreev, 2006) was recently discovered (Galuskina *et al*., 2023), some of which had a composition close to garnet of the andradite-schorlomite series, which complicated their correct identification. One of the first, qeltite (IMA2021-032), $Ca_3Ti(Fe_2Si)Si_2O_{14}$, was studied by us and approved by the CNMNC-IMA. Qeltite is the Fe-Si analog of paqueite, $Ca_3Ti(Al_2Ti)Si_2O_{14}$ (IMA2013-53), recently described from the Allende CV3 carbonaceous chondrite (Ma *et al*., 2022) and later detected in contact facies of phosphide-bearing gehlenite paralava of the Hatrurim Complex in the wadi Zohar, Hatrurim Basin, Israel (Galuskin *et al*., 2022).

Langasite phases comprise synthetic family compounds with the general formula $A_3BC_3D_2O_{14}$, where A = Ba, Sr, Ca, Pb^{2+}, Na, K; B = Ti^{4+}, Sb^{5+}, Nb^{5+}, Ta^{5+}, Te^{6+}; C = Fe^{3+}, Co^{2+}, Mn^{2+}, Ga, Al, Ti^{4+}; D = Si, Ge^{4+}, P^{5+}, V^{5+}, As^{5+} (Mill, 2009; Lyubutin *et al*., 2011; Markina *et al*., 2019; Scheuermann *et al*., 2000). The name of this family comes from the names of the chemical elements in lantanium gallium silicate $La_2Ga_5SiO_{14}$ – one member of the family (Andreev, 2004). The first phase of the langasite-type structure with composition $Ca_3Ga_2Ge_4O_{14}$ was synthesized in 1979 (Mill and Pisarevsky, 2000). Industry requests for piezoelectric materials for middle-band monolithic BAW (bulk acoustic wave) devices prompted the synthesis of these compounds at scale (Mill and Pisarevsky, 2000). The high piezoelectric and electromechanical constants of these materials (higher than those of quartz), and the absence of phase transformation up to the melting point (e.g., 1470°C) make these materials attractive for practical applications (Tichý *et al*., 2010). At present, more than 200

synthetic compounds belonging to the langasite family are known (Markina *et al*., 2019). These compounds are interesting not only for basic investigations but also for many applications due to such functional properties as piezoelectricity, optical nonlinearity, and multiferroicity. The langasite family phases have been intensively examined in the context of their applications in bulk and surface acoustic wave devices, as well as in the field of lasers, photorefractive media, nonlinear optics and electrooptics (Markina *et al*., 2019).

In nature, only one phase with the langasite-type structure that was formed at high-temperatures – paqueite – has been found until now, and this mineral was found in a meteorite (Ma *et al*., 2022). Some low-temperature mineral phases belonging to the langasite family, such as the dugganite group minerals (trigonal, *P*321) dugganite, $Pb_3Zn_3(AsO_4)_2(TeO_6)$, a = 8.460(2) Å, c = 5.206(2) Å (Williams, 1978; Lam *et al*. 1998); joëlbruggerite, $Pb_3Zn_3(Sb^{5+},Te^{6+})As_2O_{13}(OH,O)$, a = 8.4803(17) Å, c = 5.2334(12) Å (Mills *et al*., 2009); and kuksite, $Pb_3Zn_3(PO_4)_2(TeO_6)$, a = 8.39 Å, c = 5.18 Å, formed in oxidized ore pyrite-bearing metasomatites with gold-telluride mineralization (Kim *et al*., 1990) or in the oxidation zone of silver-lead and silver-polymetallic ores (Williams, 1978; Mills *et al*. 2009). The structure of cheremnykhite, $Pb_3Zn_3(VO_4)_2(TeO_6)$, which belongs to the dugganite group, needs re-investigation, as along with the structure of kuksite, it was defined as orthorhombic (a = 8.58(3) Å, b = 14.86(5) Å, c = 5.18(3) Å, Kim *et al*., 1990). The structure of joëlbruggerite should also be clarified, as the OH position was incorrectly determined as a result of the BVS miscalculation (Mills *et al*., 2009). By analogy with the formula of langasite, which was adapted to paqueite and qeltite, the crystal chemical formula of minerals of the dugganite group should be written as follows: (for example, for dugganite) $Pb_3Te^{6+}Zn_3As^{5+}{}_2O_{14}$.

There is another interesting mineral, taikanite, $Sr_2BaMn^{3+}{}_2(Si_4O_{12})O_2$, which was found in oxidized manganese ore (Kalinin *et al*., 1985). The structure of taikanite is monoclinic (*C*121,

a = 14.600(2) Å, b = 7.759(4) Å, c = 5.142(1) Å, β = 93.25(2)°) and derived from structures of the langasite type $A_3BC_3D_2O_{14}$, where the A site is split and occupied by Ba and Sr, and one of the tetrahedral sites D changes into an octahedral one and is occupied by Mn^{3+} (Armbruster *et al*., 1993).

In this paper we described qeltite – one of the terrestrial minerals with a langasite-type structure which has been discovered in paralava of the Hatrurim pyrometamorphic Complex. The mineral is named after the Wadi Qelt in the close vicinity of the qeltite type locality Nabi Musa, Judean Desert, Palestine. Type material was deposited in the mineralogical collection of the Fersman Mineralogical Museum, Leninskiy pr., 18/k2, 115162 Moscow, Russia, catalogue numbers 5695/1.

Experimental methods

The crystal morphology, optical properties and chemical composition of qeltite and associated minerals were studied using an optical microscope, a Phenom XL analytical scanning electron microscope (Institute of Earth Sciences, Faculty of Natural Sciences, University of Silesia, Sosnowiec, Poland), and an electron microprobe analyser (Cameca SX100, Micro-Area Analysis Laboratory, Polish Geological Institute - National Research Institute, Warsaw, Poland). The microprobe chemical analyses were performed in WDS mode at acceleration voltage 15 kV, beam current 20 nA, and beam diameter 1 μm. The following lines and standards were used: Mg$K\alpha$ - diopside, Si$K\alpha$ and Zr$L\alpha$ - zircon, Al$K\alpha$ and K$K\alpha$ - orthoclase, Ca$K\alpha$ - wollastonite, Sr$L\alpha$ - celestine, Nb$L\alpha$ - metallic Nb, Ba$L\beta$ - baryte, Ti$K\alpha$ - rutile, V$K\alpha$ - metallic V, Cr$K\alpha$ - Cr_2O_3, Mn$K\alpha$ - rhodonite, Fe$K\alpha$ - pentlandite, Ni$K\alpha$ - nickeline, Cu$K\alpha$ - chalcopyrite, Zn$K\alpha$ - ZnS.

Raman spectra of qeltite were recorded on a WITec alpha 300R Confocal Raman Microscope (Department of Earth Science, University of Silesia, Poland) equipped with an

air-cooled solid laser (488 nm) and a CCD camera operating at –61°C. The laser radiation was coupled to a microscope through a single-mode optical fibre with a diameter of 3.5 μm. An air Zeiss LD EC Epiplan-Neofluan DIC-100/0.75NA objective was used. Raman scattered light was focused by a broad-band single mode fibre with effective pinhole size about 30 μm and a monochromator with a 1800 gr/mm. The power of the laser at the sample position was ~ 20 mW. Integration times of 3 s with an accumulation of 20 scans and a resolution of 2 cm^{-1} were chosen. The monochromator was calibrated using the Raman scattering line of a silicon plate (520.7 cm^{-1}).

Single-crystal X-ray studies were carried out with a four-circle SuperNova diffractometer with Ag*K*α radiation (λ = 0.56087Å), equipped with an Eos CCD detector (Agilent). The detector-to-crystal distance was 66.0 mm. Ag*K*α radiation (λ=0.0560 Å) was used at 65 kV and 0.6 mA. Crystals were attached to a non-diffracting MiTeGen micromount support. A frame-width of 1° in ω scans and a frame time of 90 s were used for data collection. Reflection intensities were corrected for Lorentz, polarisation and absorption effects and converted to structure factors using CrysAlisPro 1.171.40.67a (Rigaku Oxford Diffraction, 2019) software. Observed unit-cell parameters are consistent with trigonal symmetry. The statistical tests on the distribution of |*E*| values ($|E^2-1| = 0.729$). The suggested space group symmetry was *P*321 The crystal showed significant systematic absences violations of the glide planes and screw axes. Further examination of structural model of lower, *P*3 symmetry led to model equivalent to a *P*321 structure. Scattering curves for neutral atoms were taken from the International Tables for Crystallography (Prince, 2004). The following curves were used: Ca at the *A* site; Ti at the *B* site; Fe vs Si at the *C* site; Si at the *D* site and O at the O1–O3 sites. The *A*, *B*, *D*, and O sites were found to be fully occupied by Ca, Ti, Si and O, respectively. The *C* site has a mixed (Fe,Si) occupancy. The CIF has been deposited with the Principal Editor of Mineralogical Magazine and is available as Supplementary material.

X-ray powder diffraction data for qeltite could not be measured, therefore we present a calculated powder pattern (Cu*K*a radiation, Debye-Scherrer geometry), based on the obtained structure model (Table S1). The Table S1 has been deposited with the Principal Editor of Mineralogical Magazine and is available as Supplementary material.

Qeltite occurrence and description

Qeltite was found in gehlenite-rankinite paralava within the pyrometamorphic Hatrurim Complex, which is a unique geological object described in numerous publications by different authors (Bentor *et al*., 1963a, b; Gross, 1977; Vapnik *et al.,* 2007; Geller *et al.,* 2012; Novikov *et al.,* 2013; Galuskina *et al.,* 2014), so here we provide only a brief characterization.

Rocks of the Hatrurim Complex are mainly represented by spurrite and fluorapatite marbles, gehlenite, larnite and spurrite rocks, which form large areas in the immediate surroundings of the Dead Sea Rift on the territories of Israel, Palestine and Jordan (Bentor *et al*., 1963a, b; Gross, 1977; Burg *et al*., 1991, 1999; Novikov *et al*., 2013; Khoury *et al*., 2016). Paralavas of different composition occur within pyrometamorphic rocks of the Complex (Vapnik *et al*., 2007), among them gehlenite-wollastonite-rankinite oxidized paralavas, in which qeltite was discovered and which contain only Fe^{3+}-bearing minerals (Galuskin *et al*., 2022). Rarely, reduced phosphide-bearing gehlenite and diopside paralavas are encountered (Britvin *et al*., 2015; Galuskin *et al*. 2023). The genesis of the Hatrurim Complex rocks remains enigmatic and is considered an unsolved problem (Galuskina et al. 2014). Two proposed hypotheses – the "classic" hypothesis, assuming that pyrometamorphic transformation was driven by dispersed organic matter in sedimentary protolith (Burg *et al*., 1991, 1999), and the "mud volcanos" hypothesis, proposing the participation of methane in the activation of the combustion processes (Sokol *et al*., 2010; Novikov *et al*., 2013) – cannot explain a number of geological particularities of the Complex, such as thick almost

homogeneous beds of pyrometamorphic rocks extending across a dozen square kilometers. Pyrometamorphic rocks of the Hatrurim Complex are characterized by an extraordinary variety of minerals caused by the reactions of combustion by-products (gases, fluids, melts) with earlier minerals of the clinker association and altered country rocks (Galuskin *et al*., 2016).

The qeltite-type locality "Nabi Musa", near the Palestinian village Nabi Musa, lies close to a historical place with the same name (probably the Tomb of Moses), situated in the Judean Desert, West Bank, Palestine (31°48′N/35°25′E) (Fig. 1). Nabi Musa is one of several localities of the Hatrurim Complex located in the Judean Desert in the vicinity of the Jerusalem-Jericho highway, and most of the outcrops are at the road truncation (Fig. 1a). According to Sokol *et al*. (2010), Nabi Musa locality is a huge crater-like structure. A massive, brecciated fragment of pyrometamorphic rocks, mainly larnite, gehlenite, spurrite, are embedded in altered rock represented by zeolitic and calcium silicate hydrated rocks. Small paralava bodies form veins and nests up to 0.15 m long (Fig. 1b). Paralava containing qeltite is composed of rankinite, gehlenite, rarer wollastonite, Ti-bearing andradite, and kalsilite. Minerals of the khesinite-dorrite series, barioferrite, minerals of magnesioferrite-magnetite-maghemite series, hematite, Si-bearing perovskite, Si-V-bearing fluorapatite, gurimite, hexacelsian and an unidentified Ca-U-silicate are accessory minerals (Fig. 2). Baryte, hydrated calcium silicates such as tobermorite, afwillite, tacharanite, and fabrièsite-like mineral are later, hydrothermal minerals.

Later, qeltite was detected in paralava at two localities in the Hatrurim Basin in the Negev Desert in Israel. The first locality is placed in the upper reaches of a tributary of the Halamish Wadi. Here, qeltite with composition

$(Ca_{2.95}Sr_{0.02}Ba_{0.01}Mn_{0.01})_{\Sigma 2.99}Ti^{4+}Si_2(Fe^{3+}_{1.55}Si_{0.57}Al_{0.46}Ti^{4+}_{0.42}Cr_{0.01})_{\Sigma 3.01}O_{14}$

was found in gehlenite-wollastonite-Ti-bearing andradite paralava, which also contains a significant amount of fluorapatite-fluorellestadite group minerals. Andradite and åkermanite are minor minerals, and khesinite, barioferrite, magnesioferrite, dorrite, and perovskite are accessory minerals in this rock. Another locality with rankinite-gehlenite-Ti-bearing andradite paralava containing qeltite, $(Ca_{2.96}Sr_{0.03}Ba_{0.01})_{\Sigma 3}Ti^{4+}Si_2(Fe^{3+}_{1.44}Al_{0.58}Si_{0.55}Ti^{4+}_{0.44})O_{14}$, and its Ti-analogue, $Ca_3Ti^{4+}Si_2(Fe^{3+}_{1.27}Al_{0.76}Ti^{4+}_{0.55}Si_{0.34})O_{14}$, is located 700 m to the left of road no. 31 Arad-Dead Sea. Wollastonite, kalsilite, and akermanite are occasionally observed in this paralava. Barioferrite, magnesioferrite, perovskite, khesinite, fluorapatite, aradite, gurimite, Ba-U-perovskite are accessory minerals.

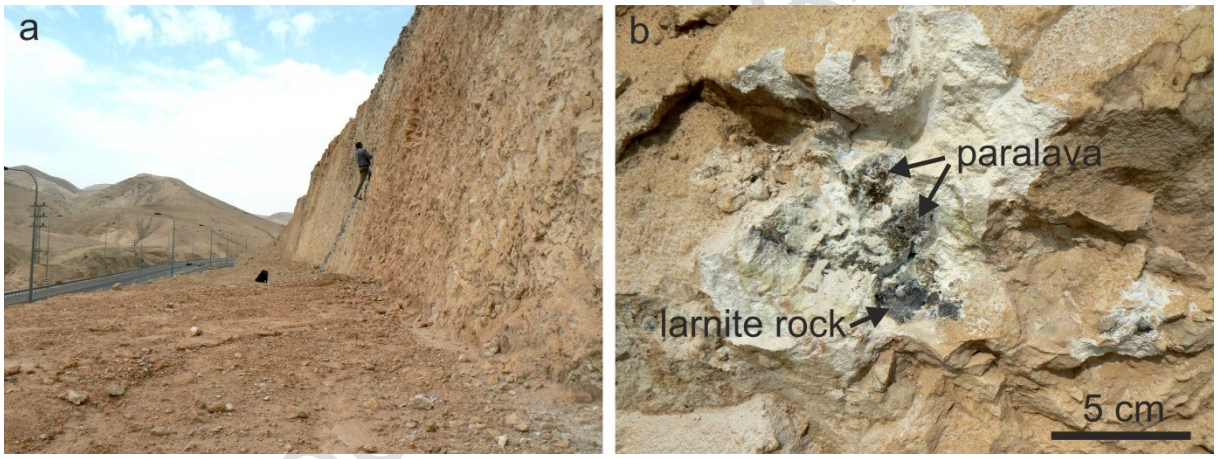

Fig. 1. (a) Nabi Musa locality along the Jerusalem-Jericho highway truncation. (b) Gehlenite-rankinite-wollastonite paralava nest in altered hydrogrossular-bearing rock.

Qeltite generally forms aggregates of flattened crystals up to 40–50 μm in length and less than 5 μm in thickness. These aggregates occur in small enclaves 100–200 μm in size in rankinite (Fig. 2a-c). Rarely, tabular qeltite crystals with inclusions of fluorapatite (Fig. 2d) and hematite (Fig. 2e) more than 100 μm in length and about 10 μm in thickness are noted. In optical images it is clear that qeltite exhibits a light-brown color with a red hue (Fig. 3b). It has a yellowish-white streak and a vitreous to subadamantine lustre. Its microhardness VHN_{25}

is 708(17) kg/mm^2, average of 22 measurements, range 683–738 kg/mm^2. It has a hardness of about 6 on the Mohs scale. Cleavage and parting are not observed. The mineral is brittle. It displays an uneven and conchoidal fracture. It is not magnetic. Qeltite is uniaxial (+), its refractive indexes are $\omega \approx 1.85$, $\varepsilon \approx 1.90$, $\Delta \approx 0.05$, and its mean calculated refractive index is 1.871, $\varepsilon = C$ ($\lambda = 589$ nm). It exhibits pleochroism, as it is light-colored, pink along Z and intensively-colored, red-brown along X/Y (Fig. 3b, c). The density of qeltite was not measured because of the small size of its crystals. Its calculated density is 3.48 g·cm^{-3} based on the empirical formula and unit cell volume refined from the SC-XRD data. The Gladstone-Dale compatibility index is $1 - (K_P/K_C) = 0.030$ (excellent) (Mandarino, 1989).

The results of the electron microprobe analyses of qeltite are given in Table 1.

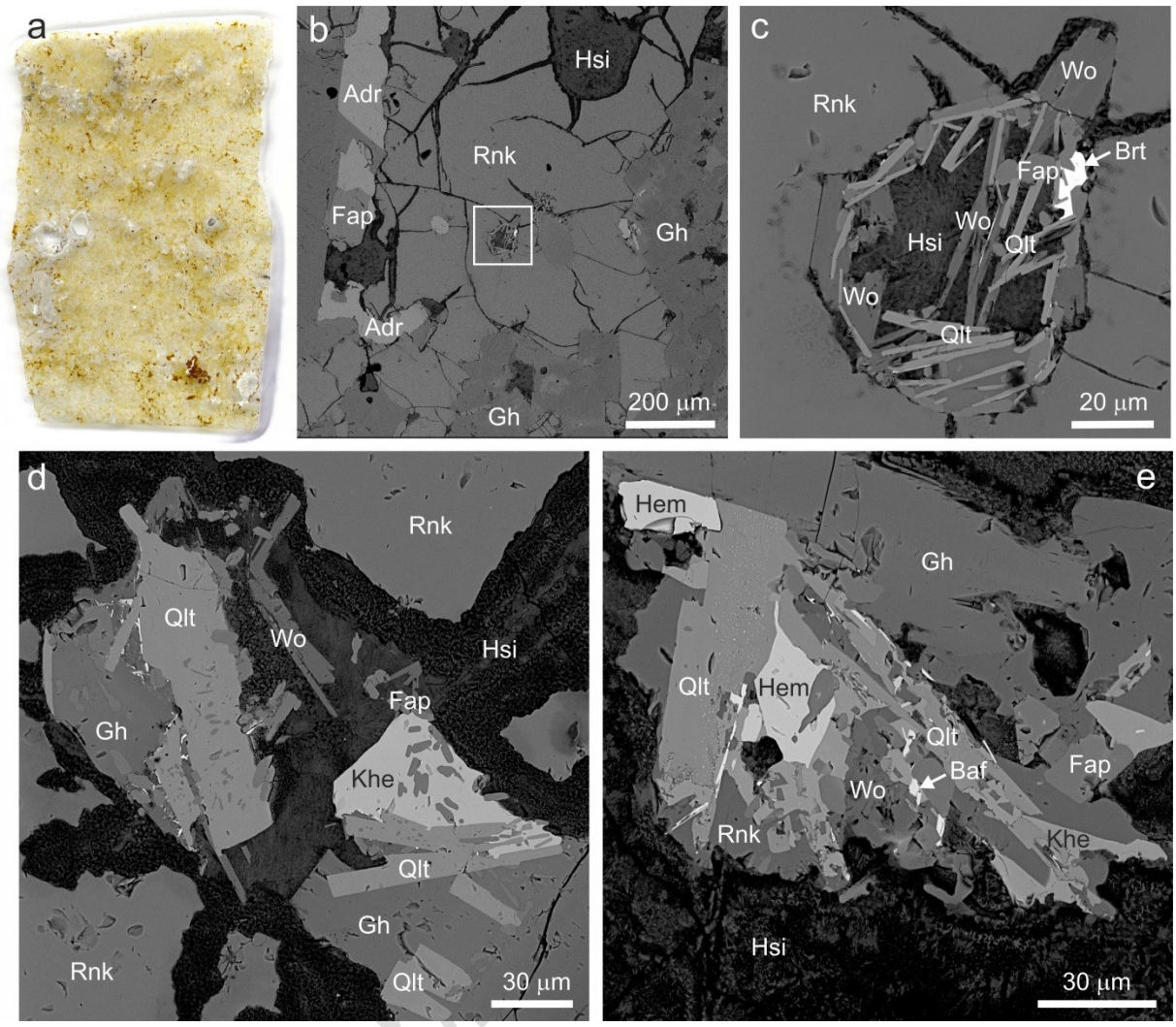

Fig. 2. (a) Thin-section made from paralava of the type locality specimen containing qeltite, yellow – gehlenite, brown – Ti-bearing andradite, white, transparent – rankinite, wollastonite, hydrated calcium silicates. (b) Qeltite is in small enclaves inside rankinite grains; the fragment magnified in Fig. 2c is shown in the frame. (c) Flattened qeltite crystals. (d, e) Typical mineral association containing qeltite crystals. Qeltite often contains fluorapatite inclusions (d) and very small inclusions of hematite (e). (b-e) BSE images.

Adr – Ti-bearing andradite, Baf – barioferrite, Brt – baryte, Hem – hematite, Hsi – calcium hydrated silicate, Fap – fluorapatite, Gh – gehlenite, Khe – khesinite, Qlt – qeltite, Rnk – rankinite, Wo – wollastonite. The abbreviations are after Warr (2021).

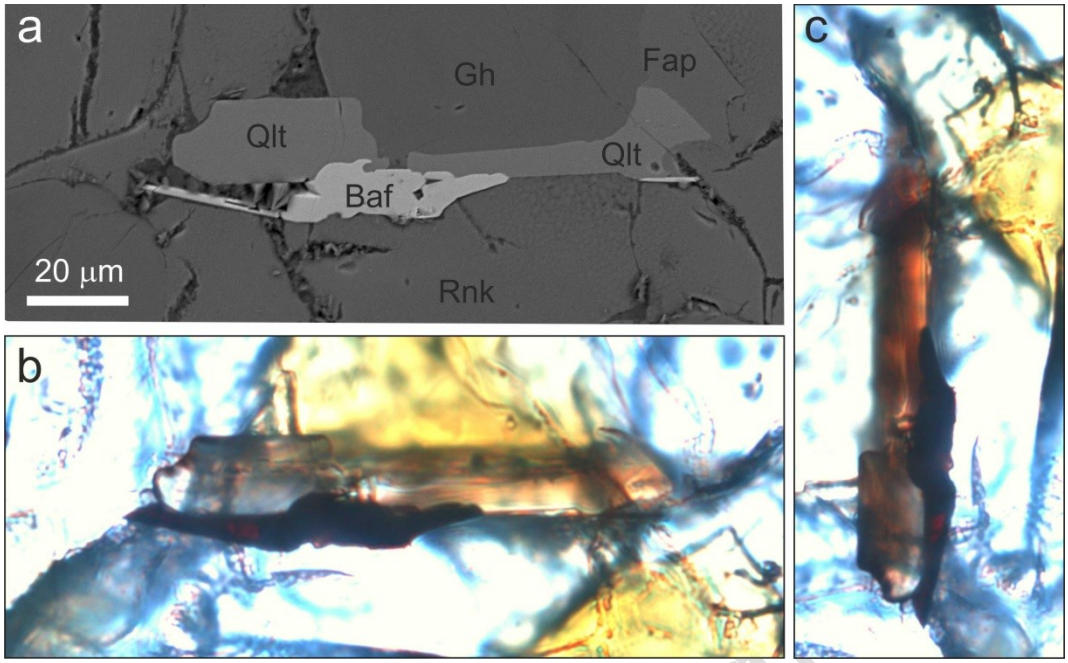

Fig. 3. (a) BSE image of qeltite crystal. (b-c) Optical images of the same qeltite crystal showing pleochroism changing from light-brown (~ ∥ *Z*) to dark-brown with a red hue (~⊥ *Z*). Baf – barioferrite, Fap – fluorapatite, Gh – gehlenite, Qlt – qeltite, Rnk – rankinite. The abbreviations are after Warr (2021).

The studied qeltite is characterized by significant Ti and Al content (Table 1). The empirical formulas of qeltite, $(Ca_{2.96}Sr_{0.02}Mn^{2+}_{0.01})_{\Sigma 2.99}(Ti^{4+}_{0.99}Cr^{3+}_{0.01})_{\Sigma 1.00}(Fe^{3+}_{1.59}Si_{0.60}Al_{0.43}Ti^{4+}_{0.39})_{\Sigma 3.01}(Si_{1.99}P_{0.01})_{\Sigma 2.00}O_{14}$ (grain used for SC-XRD) and $(Ca_{2.96}Sr_{0.02}Ba_{0.01}\ Mn^{2+}_{0.01})_{\Sigma 3.00}$ $(Ti^{4+}_{0.96}Cr^{3+}_{0.03}Zr_{0.01})_{\Sigma 1.00}(Fe^{3+}_{1.53}Si_{0.63}Al_{0.46}Ti^{4+}_{0.38})_{\Sigma 3.01}(Si_{1.98}P_{0.02})_{\Sigma 2.00}O_{14}$ (Table 1, taking into account the dominant valence rule and possibility of double occupation at one structural site, can be simplified to $Ca_3Ti(Fe^{3+}_2Si)Si_2O_{14}$. The content of the paqueite end-member, $Ca_3Ti(Al_2Ti)Si_2O_{14}$, in qeltite varies in the limits 21–23%.

Raman spectroscopy

The features of the Raman spectra of qeltite depend on the crystal orientation (Fig. 4). The Raman spectrum of qeltite differs from the spectra of typical nesosilicates (for example, minerals of the garnet and schorlomite groups) by the fact that the strongest band in the qeltite spectrum at 611–613 cm^{-1} is related to the symmetric stretching vibration of Ti-O in the $^{B}(TiO_6)^{8-}$ octahedron (Frank *et al.*, 2012; Vásquez *et al.*, 2017; Su *et al.*, 2000; Heyns *et al.*, 2000). The bands of lower intensities are complex and are mainly connected with vibrations of Si-O, Fe^{3+}-O, Al-O and Ti^{4+}-O bonds at the tetrahedral sites *C* and *D*. The main bands in the qeltite Raman spectrum are as follows (Fig. 4, cm^{-1}, ~⊥Z/∥Z): 166/172, 218/215 related to Ca-O vibrations and/or $\nu_2{}^{B}(TiO_6)^{8-}$; 244/252, 331/~353 related to the vibrations $R(TO_4)$, $\nu_2{}^{C}(FeO_4)^{5-}$; 437/448 – $\nu_4{}^{B}(TiO_6)^{8-}$, $\nu_4{}^{C}(FeO_4)^{5-}$, $\nu_4{}^{D}(SiO_4)^{4-}$; 611/613 – $\nu_1{}^{B}(TiO_6)^{8-}$, $\nu(^{B}Ti\text{-}O\text{-}^{D}Ti)$; 713/718 – $\nu_1{}^{D}(FeO_4)^{5-}$; 766 – $\nu_1{}^{C}(TiO_4)^{4-}$, $\nu_1{}^{C}(AlO_4)^{5-}$; 855 – $\nu_1{}^{D}(SiO_4)^{4-}$; 978/986 – $\nu_3{}^{D}(SiO_4)^{4-}$, $\nu(^{C}Si\text{-}O\text{-}^{D}Si)$. The interpretation of bands was carried out based on Raman data obtained by different authors for TiO_2 polymorphs, Ti-bearing garnets, titanite and other titanosilicates (Galuskina *et al.*, 2005; Frank *et al.*, 2012; Vásquez *et al.*, 2017; Su *et al.*, 2000; Heyns *et al.*, 2000).

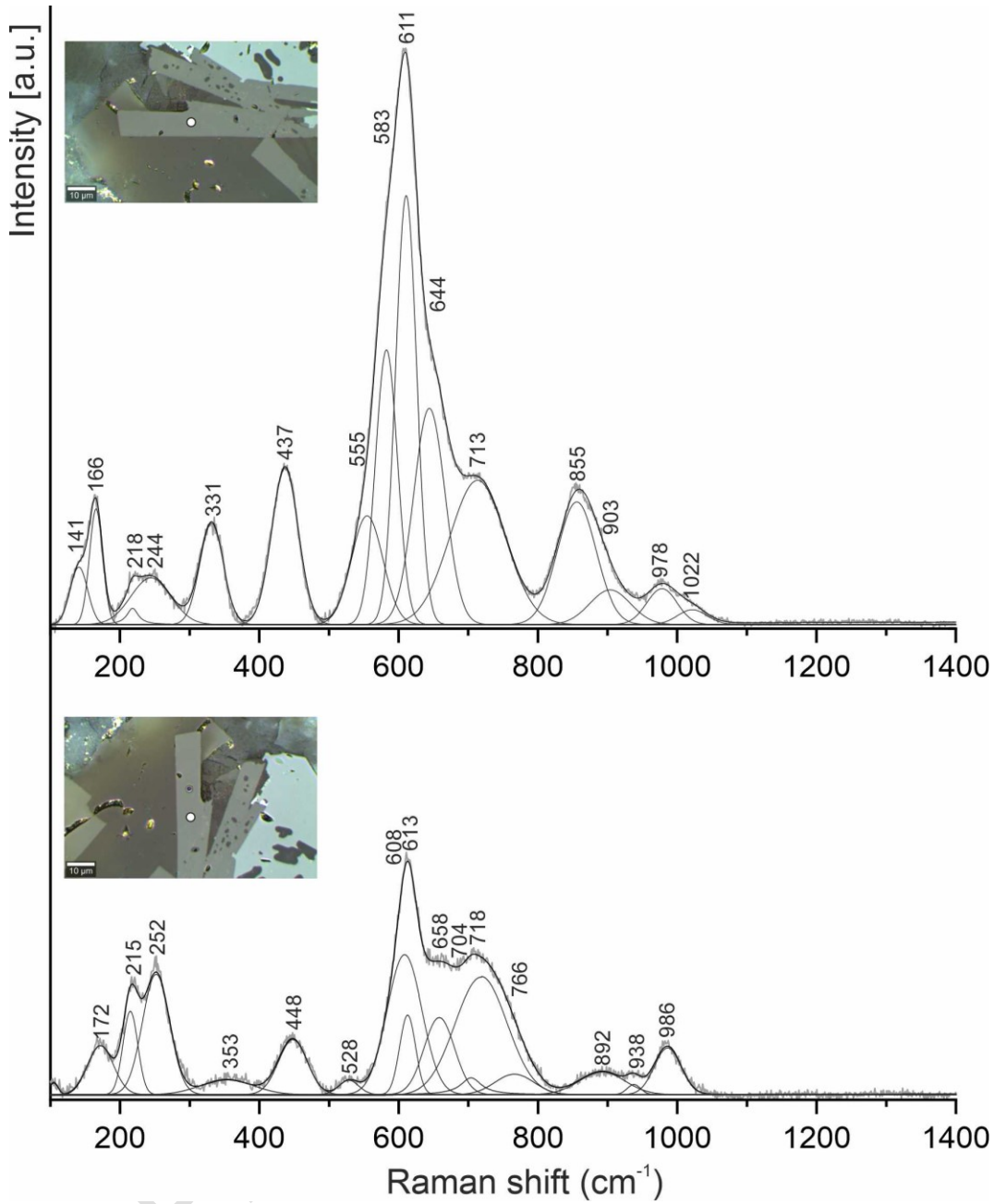

Fig. 4. Raman spectra of qeltite on different orientations of crystal.

Crystallography

Structural data were obtained for a 0.042 × 0.019 × 0.013 mm^3 crystal at 295.5(4) K. Experimental data and the results of structure refinement are given in Tables 2–5. Bond valence sum (BVS) calculations are shown in Table 6.

Qeltite, $Ca_3Ti(Fe^{3+}{}_2Si)Si_2O_{14}$ [*P*321, $a = b = 8.0077(5)$, $c = 4.9956(4)$ Å], belongs to the langasite structural type – a family of synthetic compounds with the general formula $A_3BC_3D_2O_{14}$ (Mill, 2009; Marty *et al*., 2010; Lyubutin *et al*., 2011; Markina *et al*,., 2019). Paqueite, $Ca_3TiSi_2(Al_2Ti)O_{14}$ (there are only EBSD data; the structural model is the langasite-type synthetic phase $Ca_3TiSi_2(Al,Ti,Si)_3O_{14}$: *P*321, $a = b = 7.943$, $c = 4.930$ Å; Scheuermann *et al*., 2000), is known to exist in nature, as it has been described in meteorites (Paque *et al*., 1994; Ma and Beckett, 2016). Qeltite, $Ca_3Ti(Fe^{3+}{}_2Si)Si_2O_{14}$, is a Fe^{3+}-analog of paqueite, at the *D*-tetrahedra of which $Si > Ti^{4+}$ (Table 5). The qeltite structure belongs to the trigonal non-centrosymmetric *P*321 space group. In qeltite, CaO_8 polyhedra and TiO_6 octahedra form a layer in which the central TiO_6 octahedron shares three edges with three CaO_8 polyhedra. These CaO_8 polyhedra are further connected to other CaO_8 polyhedra by corner sharing (Fig. 5, 6). The CaO_8 polyhedra are distorted, with bond lengths ranging from 2.358(5) to 2.868(4) Å. In fact, Ti at coordination 6 is at the centrum of a truncated trigonal trapezohedron with the distances Ti-O(3) = 1.954(5). In adjacent layers, SiO_4 tetrahedra share three corners (O1-atoms) with larger $[(Fe^{3+},Al)_2(Si,Ti)]O_4$ *C*-tetrahedra. The base of the SiO_4 tetrahedron has three longer bond-lengths of 1.638(4) Å to O1-atoms and one shorter bond-length of 1.584(8) Å to O2, which connects the SiO_4 tetrahedra to three CaO_8 polyhedra from the next layer. These relatively weak Ca-O2 bonds of 2.645(3) Å contribute to the underbonding of O2 (Table 6). The limited degree of positional freedom (O2 lies on a three-fold axis, 2*d* Wyckoff position) prevents from releaving this underbonding. Thus, the bonding deficiency is relieved by remaining O atoms that show little overbonding (Table 6). Bond-valence sum averaged over all anions per formula unit averages ideally to 2.00 valence units.

The $[(Fe^{3+},Al)_2(Si,Ti)]O_4$ tetrahedron has two shorter bonds of 1.791(5) to O3-atoms, connecting this tetrahedron to the TiO_6 octahedra, and two longer bonds of 1.883(4) to O1-atoms, connecting this tetrahedron to the CaO_8 polyhedra. We included two additional weak

interactions of *C*-site cations to O3, distant by 2.564(6) Å, which contribute to O2 underbonding compensation. The obtained structural formula of qeltite $Ca_{3.00}Ti(Fe_{1.75}Si_{1.25})_{\Sigma 3.00}Si_{2.00}O_{14}$, which is charge balanced due to the substitution of part of Fe^{3+} and Si by Ti^{4+} and Al at the *C* site, and the empirical formula, $(Ca_{2.96}Sr_{0.02}Mn^{2+}_{0.01})_{\Sigma 2.99}(Ti^{4+}_{0.99}Cr^{3+}_{0.01})_{\Sigma 1.00}(Fe^{3+}_{1.59}Si_{0.60}Al_{0.43}Ti^{4+}_{0.39})_{\Sigma 3.01}(Si_{1.99}P_{0.01})_{\Sigma 2.00}O_{14}$, are well-matched. The number of electrons for the *C*-tetrahedron in the structural formula is 20.96 and 21.30 electrons in the qeltite empirical formula calculated from the basis microprobe analyses.

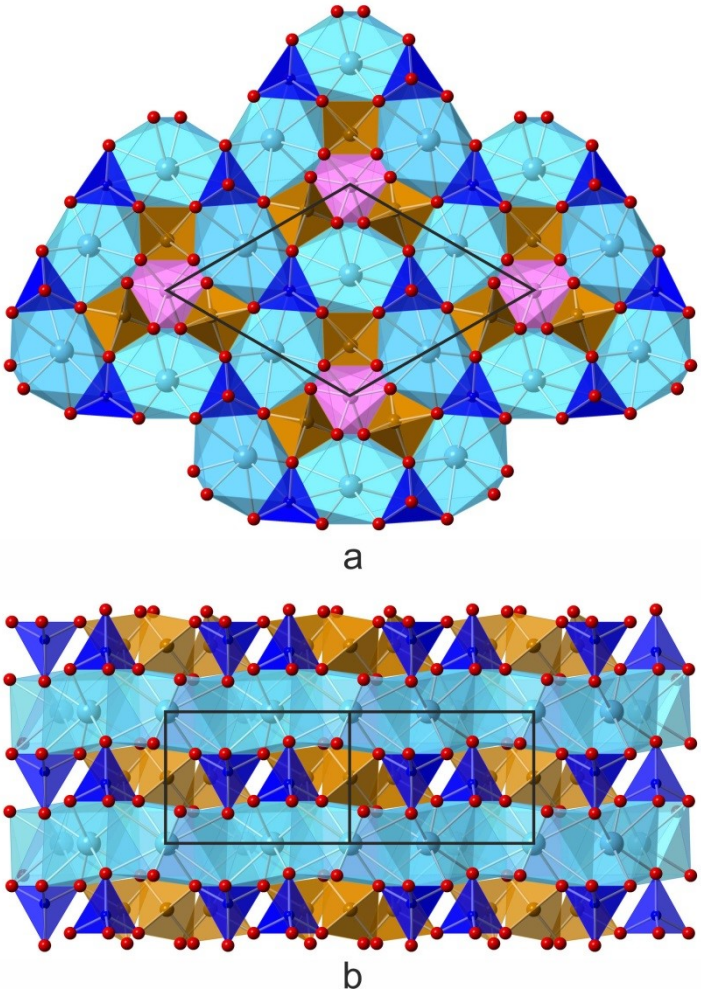

Fig. 5. Structure of qeltite. (a) projection on (001), (b) projection on (100). Unit cell is shown by black line. Ca-polyhedra – blue, Ti-octahedra – pink, Si-tetrahedra – navy blue, Fe-tetrahedra – light-brown.

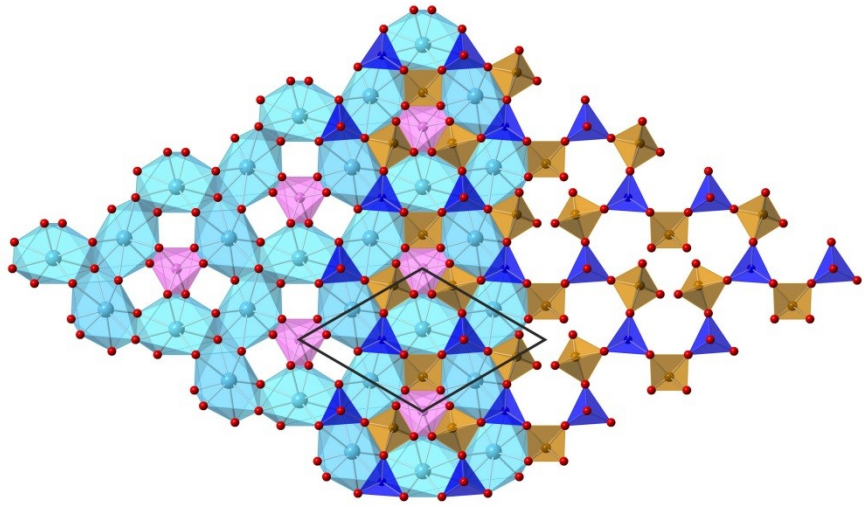

Fig. 6. Projection of qeltite structure on (001). Two layers – polyhedral (z = 0) and tetrahedral (z = ½) in the qeltite structure are shown. Unit cell is shown by the black line. Ca-polyhedra – blue, Ti-octahedra – pink, Si-tetrahedra – navy blue, Fe-tetrahedra – light-brown.

Discussion

In the last few years, a number of mineral phases with the langasite-type structure and different composition with the general formula $A_3BC_3D_2O_{14}$, where A = Ca and Ba; B = Ti, Nb, Sb, and Zr; C = Ti, Al, Fe, and Si; and D = Si, have been detected in pyrometamorphic rocks of the Hatrurim Complex. Among them are minerals close in composition to titanian garnet of the andradite-schorlomite series – for example, qeltite, $Ca_3Ti^{4+}(Fe^{3+}{}_2Si)Si_2O_{14}$, as described in this article – and minerals with exotic composition such as $Ba_3Nb^{5+}Fe^{3+}{}_3Si_2O_{14}$. We consider that the systematics and nomenclature of minerals with langasite-type structure (duggenite supergroup) should be elaborated after the full study of the minerals found in the Hatrurim Complex rocks (Galuskina *et al*., 2023).

Following the discovery of qeltite in paralava of Nabi Musa locality, Palestine, it turned out that isostructural minerals with the common composition $Ca_3Ti\,(Fe^{3+},Al,Si,Ti^{4+})_3Si_2O_{14}$ are widely distributed in the paralavas of the Hatrurim Basin,

Israel and often associate with garnets of the andradite-schorlomite series, which are similar by composition. In Ti-bearing garnets, $Ca_3(Fe^{3+},Al\ldots,Ti^{4+})_2(Si,Fe^{3+},Al)_3O_{12}$ an entry of Ti^{4+} at the octahedral site is facilitated by the substitution of some Si by trivalent cations at the tetrahedral site: $^{VI}(Fe^{3+}, Al\ldots)^{IV}Si \rightarrow {}^{VI}(Ti^{4+})^{IV}(Fe^{3+},Al)$. In qeltite, $Ca_3Ti(Fe^{3+}{}_2Si)Si_2O_{14}$, Ti^{4+} occupies the octahedral site and can enter the tetrahedral site, replacing Si. Increasing Fe^{3+}, Al content at the tetrahedral site to more than 2 apfu can be related to the presence of Nb^{5+} or Sb^{5+} at the octahedral site according to the isomorphic scheme $^{VI}(Ti^{4+})^{IV}(Si,Ti^{4+})\rightarrow{}^{VI}(Nb^{5+},Sb^{5+})^{IV}$ (Fe^{3+},Al) (Galuskina *et al.*, 2023). The appearance of Ti^{4+} at the tetrahedral coordination is an exceedingly rare phenomenon, and this has also been noted in Si, Al-deficient pyroxenes and amphiboles (Carbonin *et al.*, 1989; Oberti *et al.*, 1992). Titanium in qeltite shares a site coordinated by O1×2 (M-O = 1.883 Å) and O3×2 (M-O = 1.791 Å) with Al, Si, Fe^{3+}, for which the tetrahedral coordination is usual. The *C* site can be considered 4+2 coordinated, as two O3 atoms are at 2.564 Å from the center of the tetrahedron (Table 5). The effect of these two additional oxygens on the cation at the *C* site is relatively insignificant in the case of Si and Al, but in the case of Fe^{3+} and Ti^{4+} the effect is noticeable (Table 6). A unique aspect of qeltite structure (close to the composition of isostructural minerals) consists in the wide isomorphism of cations at the *C* tetrahedral site, including Ti^{4+}, for which this coordination is atypical. We consider that the entry of Ti^{4+} (and other large cations) at the *C* site is simplified by a change of its coordination to 4+2 (octahedral). It is likely that qeltite has a domain structure due to the significant differences among the cation sizes of the *C*-site.

The Ti^{4+} site coordinated by six oxygens is usually called the octahedral site. However, a more accurate description would be a trigonal trapezohedron truncated by a pinacoid, which has left and right forms. Comparison of the structures of paqueite and qeltite shows that they are right and left forms of the archetypal langasite structure (Galuskina *et al.*, 2023). It is

interesting that the qeltite space group *P*321 does not have screw axes, which are a necessary condition for the appearance of enatiomorphic forms (Fecher *et al*., 2022). Chirality in phases with the langasite-type structure is related to the effects of specific structural disordering in the distribution of electron density, which leads to the formation of a pseudoscrew axis with the period 3*c* (Dudka and Mill, 2014).

Qeltite in paralava is usually confined to small oval aggregates of fine-grained minerals against a coarse-grained background of rock-forming minerals (Fig. 2b,c). As a rule, these aggregates are enriched in elements that are incompatible with rock-forming minerals, such as Ti, Fe, Ba, U, V, Nb, and others (Galuskina *et al*., 2017a). In similar aggregates, a series of new minerals and varieties characterized by unusual composition and structure, such as hexacelsian, $BaAl_2Si_2O_8$, zadovite, $BaCa_6[(SiO_4)(PO_4)](PO_4)_2F$, aradite, $BaCa_6[(SiO_4)(VO_4)](VO_4)_2F$, gurimite, $Ba_3(VO_4)_2$, mazorite, $Ba_3(PO_4)_2$, bennesherite, $Ba_2Fe^{2+}[Si_2O_7]$, uranium-bearing cuspidine, $Ca_8(Si_2O_7)_2F_4$, vorlanite, $Ca(U^{6+})O_4$, and khesinite, $Ca_4(Mg_3Fe^{3+}_9)O_4(Fe^{3+}_9Si_3)O_{36}$, has been described. Previously, we interpreted similar aggregates as a crystallization of minerals from residual melt (liquid) enriched with incompatible elements, which remained between crystals of pre-existing rock-forming minerals. The studied paralavas have no flow structures and are completely crystallized, and the size of rock-forming minerals reaches more than 1 cm. These aggregates rather resemble pegmatites and veins, in which minerals crystallize in a particular direction from the walls of a cavity. We also cannot exclude the possibility that the enrichment of small fragments of paralava is conditioned upon the inhomogeneity of protolith and weakly homogenized melt. If such assumption is valid, the aggregates with Ba, U, Fe-Ti, V mineralization should be interpreted as refractory inclusions like those which occur in meteorites. The Ti-Al-analog of qeltite – paqueite, $Ca_3Ti(Al_2Ti)Si_2O_{14}$ – has been described in such inclusions (Ma *et al*., 2022). Khesinite, a mineral analogue of the SCFA phase, which appears in products of the

calcination of iron ore at temperatures above 1200°C (Galuskina *et al*., 2017b), occurs in association with qeltite. The temperature of crystallization of paqueite in association with iron phosphides, osbornite and pseudowollastonite from explosive breccia of the Hatrurim Complex in Israel was higher than 1250°C (Galuskin *et al*., 2022). Similarly, the temperature of qeltite crystallization in paralava was about 1200°C. High-temperature and near-surface conditions of qeltite genesis probably defines its absence in terrestrial magmatic and metamorphic rocks, which contain widely distributed Ti-rich garnets close to it in composition. Nevertheless, intimate intergrowths of qeltite with Ti-garnets in paralavas of the Hatrurim Complex indicate that the conditions for its crystallization can be realized in high-temperature magmatic systems of defined composition.

ACKNOWLEDGMENTS

The authors thank Peter Leverett, Sergey Britvin and the anonymous Reviewer for their careful revision and useful comments that improved an early version of the manuscript. Investigations were supported by the National Science Center of Poland [grant number 2021/41/B/ST10/00130 (E.G., I.G.) and grant number 2019/33/ B/ST10/02671 (K.W.)].

REFERENCES

Andreev, I.A. (2004) Two decades following the discovery of thermally stable elastic properties of $La_3Ga_5SiO_{14}$ crystal and coining of the term “Langasite” (A Review). *Zhurnal Tekhnicheskoi Fiziki*, **74**(9), 1–3.

Andreev, I.A. (2006) Single crystals of the langasite family: an intriguing combination of properties promising for acoustoelectronics. *Technical Physics*, **51**(6), 758–764.

Armbruster, T., Oberhänsli, R., and Kunz. M. (1993) Taikanite, $BaSr_2Mn^{3+}{}_2O_2[Si_4O_{12}]$, from the Wessels mine, South Africa: a chain silicate related to synthetic $Ca_3Mn^{3+}{}_2O_2[Si_4O_{12}]$. *American Mineralogist*, **78**, 1088–1095.

Belokoneva, E.L., Simonov, M.A., Butashin, A.V., Mill, B.V., and Belov, N.V. (1980) Crystal structure of Ca-gallogermante $Ca_3Ga_2Ge_4O_{14}$ - $Ca_3Ge[(Ga_2Ge)Ge_2O_{14}]$ and its analog $Ba_3Fe_2Ge_4O_{14}$ - $Ba_3[(FeGe_2)Ge_2O_{14}]$. *Doklady Akademii Nauk SSSR*, **255**(5), 1099–1104.

Bentor, Y.K., Gross, S., and Heller, L. (1963a) High-temperature minerals in non-metamorphosed sediments in Israel. *Nature*, **199**, 478–479, doi:10.1038/199478a0

Bentor, Y.K., Gross, S. and Heller, L. (1963b) Some unusual minerals from the "Mottled Zone", Israel. *American Mineralogist*, **48**(7–8), 924–930.

Britvin, S.N., Murashko, M.N., Vapnik, Y., Polekhovsky, Y.S., and Krivovichev, S.V. (2015) Earth's phosphides in Levant and insights into the source of Archean prebiotic phosphorus. *Scientific Reports*, 510, Article number 8355, doi: 10.1038/srep08355

Burg, A., Kolodny, Y., and Lyakhovsky, V. (1999) Hatrurim-2000: The „Mottled Zone" revisited, forty years later. *Israel Journal of Earth Sciences*, **48**, 209–223.

Burg, A., Starinsky, A., Bartov, Y., and Kolodny, Y. (1991) Geology of the Hatrurim Formation ("Mottled Zone") in the Hatrurim basin. *Israel Journal of Earth Sciences*, **40**, 107–124.

Carbonin, S., Salviulo, G., Munno, R., Desiderio, M., and Negro, D. (1989) Crystal-chemical examination of natural diopsides: some geometrical indications of Si-Ti tetrahedral substitution. *Mineralogy and Petrology*, **41**, 1–10.

Dudka, A.P., and Mill, B.V. (2014) X-ray diffraction study of $Nd_3Ga_5SiO_{14}$ crystal at 295 and 90K and the structural basis of chirality. *Crystallography*, 59(5), 759–768.

Fecher, G.H., Kübler, J., and Felser, C. (2022) Chirality in the solid State: Chiral crystal structures in chiral and achiral space groups. *Materials*, **15**, 5812.

Flack, H.D. (1983) On Enantiomorph-Polarity Estimation. *Acta Crystallographica*, A**39**, 876-881.

Frank, O., Zukalova, M., Laskova, B., Kürti, J., Koltai, J., and Kavan, L. (2012) Raman spectra of titanium dioxide (anatase, rutile) with identified oxygen isotopes (16, 17, 18). *Physical Chemistry Chemical Physics*, **14**, 14567–14572.

Gagné, O.C., and Hawthorne, F.C. (2015) Comprehensive derivation of bond-valence parameters for ion pairs involving oxygen. *Acta Crystallographica Section B*: Structural Sciences, Crystal Engineering and Materials, **71**, 562-578.

Galuskin, E.V., Galuskina, I.O., Gfeller, F., Krüger, B., Kusz, J., Vapnik, Ye,, Dulski, M., and Dzierżanowski, P. (2016) Silicocarnotite, $Ca_5[(SiO_4)(PO_4)](PO_4)$, a new 'old' mineral from the Negev Desert, Israel, and the ternesitesilicocarnotite solid solution: indicators of high-temperature alteration of pyrometamorphic rocks of the Hatrurim Complex, Southern Levant. *European Journal of Mineralogy*, **28**, 105–123.

Galuskin, E., Galuskina, I.O., Kamenetsky, V., Vapnik, Y., Kusz, J., and Zieliński, G. (2022) First in situ terrestrial osbornite (TiN) in the pyrometamorphic Hatrurim Complex, Israel. *Lithosphere*, 2022 (1), art. no. 8127747.

Galuskina, I.O., Galuskin, E.V., Dzierżanowski, P., Armbruster, T., and Kozanecki, M. (2005) A natural scandian garnet. *American Mineralogist*, **90**(10), 1688 – 1692.

Galuskina, I.O., Galuskin, E.V., Pakhomova, A.S., Widmer, R., Armbruster, T., Krüger, B., Grew, E.S., Vapnik, Y., Dzierażanowski, P., and Murashko, M. (2017b) Khesinite, $Ca_4Mg_2Fe^{3+}_{10}O_4[(Fe^{3+}_{10}Si_2)O_{36}]$, a new rhönite-group (sapphirine supergroup) mineral from the Negev Desert, Israel - Natural analogue of the SFCA phase. *European Journal of Mineralogy*, **29**(1), 101–116.

Galuskina, I.O., Galuskin, E.V., Vapnik, Ye., Prusik, K., Stasiak, M., Dzierżanowski, P., and Murashko, M. (2017a) Gurimite, $Ba_3(VO_4)_2$ and hexacelsian, $BaAl_2Si_2O_8$ – two new minerals from schorlomite-rich paralava of the Hatrurim Complex, Negev Desert, Israel. *Mineralogical Magazine*, **81**(4) 1009–1019

Galuskina, I., Galuskin, E., and Vapnik, Ye. (2023) Not only garnet... *Lithosphere*, 2023(186), art. ID 6113232.

Galuskina, I.O., Vapnik, Ye., Lazic, B., Armbruster, T., Murashko, M., and Galuskin, E.V. (2014) Harmunite $CaFe_2O_4$: a new mineral from the Jabel Harmun, West Bank, Palestinian Autonomy, Israel. *American Mineralogist*, **99**(5–6), 965–975.

Geller, Y.I., Burg, A., Halicz, L., and Kolodny, Y. (2012) System closure during the combustion metamorphic'' Mottled Zone'' event, Israel. *Chemical Geology*, **334**, 25–36.

Gross, S. (1977) The mineralogy of the Hatrurim Formation, Israel. *Bulletin of the Geological Survey of Israel*, **70**, 1–80.

Heyns, A.M., Harden, P.M., and Prinsloo, L.C. (2000) Resonance Raman study of the high-pressure phase transition in chromium-doped titanite, $CaTiOSiO_4$. *Journal of Raman Spectroscopy*, **31**, 837–841.

Kalinin, V. V., Dauletkulov, A. B., Gorshkov, A. I., and Troneva, N. V. (1985) Taikanite - a new strontium barium manganese silicate. *Zapiski Vsesoyuznogo Mineralogicheskogo Obshchestva*, **114**(5), 635–640 (in Russian).

Kaminskii, A.A., Mill, B.V., *G.* G. Khodzhabagyan, G.G., Konstantinova, A.F., Okorochkov, A.I., and Silvestrova, I.M. (1983) Investigation of trigonal $(La_{1-x}Nd_x)Ga_5SiO_{14}$ crystals. *Physica Status Solidi* (a), **80**, 387–398.

Khoury, H.N., Sokol, E.V., Kokh, S.N., Seryotkin, Y.V., Nigmatulina, E.N., Goryainov, S.V., Belogub, E.V., and Clark, I.D. (2016) Tululite,

$Ca_{14}(Fe^{3+},Al)(Al,Zn,Fe^{3+},Si,P,Mn,Mg)_{15}O_{36}$: a new Ca zincate-aluminate from combustion metamorphic marbles, Central Jordan. *Mineralogy and Petrology*, **110**, 125–140.

Kim, A.A., Zayakina, N.V., and Makhotko, V.F. (1990) Kuksite $Pb_3Zn_3TeO_6(PO_4)_2$ and cheremnykhite $Pb_3Zn_3TeO_6(VO_4)_2$ – new tellurates from the Kuranakh gold deposit (Central Aldan, southern Yakutia). *Zapiski Vsesoyuznogo Mineralogicheskogo Obshchestva*, **119**(5), 50–57.

Lam, A.E., Groat, L.A., and Ercit, T.S. (1998) The crystal structure of dugganite, $Pb_3Zn_3Te^{6+}As_2O_{14}$. *The Canadian Mineralogist*, **36**, 823–830.

Lyubutin, I.S., Naumov, P.G., Mill', B.V., Frolov, K.V., and Demikhov, E.I. (2011) Structural and magnetic properties of the iron-containing langasite family $A_3MFe_3X_2O_{14}$ (A = Ba, Sr; M = Sb, Nb, Ta; X = Si, Ge) observed by Mössbauer spectroscopy. *Physical Review B*, **84**, Article ID 214425.

Ma, C., and Beckett, J.R. (2016) Burnettite, $CaVAlSiO_6$, and paqueite, $Ca_3TiSi_2(Al_2Ti)O_{14}$, two new minerals from Allende: clues to the evolution of a V-rich Ca-Al-rich inclusion. 47th Lunar and Planetary Science Conference, session T335, 1595.

Ma, C., Beckett, J.R., Tissot, E.L. H., and Rossman, G.R. (2022) New minerals in type A inclusions from Allende and clues to processes in the early solar system: Paqueite, $Ca_3TiSi_2(Al,Ti,Si)_3O_{14}$, and burnettite, $CaVAlSiO_6$. *Meteoritics and Planetary Science*, **57**(6), 1300–1324.

Mandarino, J.A. (1989) The Gladstone-Dale compatibility of some new mineral proposals considered by the Commission on New Minerals and Mineral Names, IMA (1983-1987). *European Journal of Mineralogy*, **1**, 123–125.

Markina, M.M., Mill, B.V., Pristáš, G., Marcin, M., Klimin, S.A., Boldyrev, K.N., and Popova, M.N. (2019) $La_3CrGe_3Be_2O_{14}$ and $Nd_3CrGe_3Be_2O_{14}$: New magnetic compounds of the langasite family. *Journal of Alloys and Compounds*, **779**, 380-386.

Marty, K., Bordet, P., Simonet, V., Loire, M., Ballou, R., Darie, C., Kljun, J., Bonville, P., Isnard, O., Lejay, P., Zawilski, B., and Simon, C. (2010) Magnetic and dielectric properties in the langasite-type compounds: $A_3BFe_3D_2O_{14}$ (*A*=Ba, Sr, Ca; *B*=Ta, Nb, Sb; *D*=Ge, Si) *Physical Review*, B**81**, 054416 _2010.

Mill, B.V. (2009) New Compounds (A = Na, K; M = Ga, Al, Fe; X = P, As, V) with the $Ca_3Ga_2Ge_4O_{14}$ structure. *Russian Journal of Inorganic Chemistry*, **54**(9), 1355–1357.

Mill, B.V., Butashin, A.V., Khodzhabagyan, G.G., Belokoneva, E.L., and Belov, N.V. (1982) Modified earth-rare gallates with the structure $Ga_3Ga_2Ge_4O_{14}$. *Doklady Akademii Nauk SSSR*, **264**(6), 1385–1389.

Mill, B.V. and Pisarevsky, Y.V. (2000) Langasite-type materials: From discovery to present state. In: *Proceedings of the 2000 IEEE/EIAInternational Frequency Control Symposium and Exhibition(Cat. No. 00CH37052)* (IEEE, Kansas City, MO, USA, 2000), 133–144.

Mills, S.J., Kolitsch, U., Miyawaki, R., Groat, L.A., and Poirier, G. (2009) Joëlbruggerite, $Pb_3Zn_3(Sb^{5+},Te^{6+})As_2O_{13}(OH,O)$, the Sb^{5+} analog of dugganite, from the Black Pine mine, Montana. *American Mineralogist*, **94**, 012–1017.

Novikov, I., Vapnik, Ye., and Safonova, I. (2013) Mud volcano origin of the Mottled Zone, South Levant. *Geoscience Frontiers*, **4**, 597–619.

Oberti, R., Ungaretti, L., Cannillo, E., and Hawthorne, F. (1992) The behaviour of Ti in amphiboles : I. Four- and six-coordinate Ti in richterite. *European Journal of Mineralogy*, **4**, 425–439.

Paque, J., Beckett, J.R., Barber, D.J., and Stolper, E. (1994) A new titanium-bearing calcium aluminosilicate phase: I. Meteoritic occurrences and formation in synthetic systems. *Meteorites*, **29**, 673–682.

Parson, S., Flack, H.D., and Wagner, T. (2013) Use of intensity quotients and differences in absolute structure refinement. *Acta Crystallographica Section B*: Structural Sciences, Crystal Engineering and Materials, **69**, 249-259.

Prince, E. (2004) International Tables for Crystallography, volume C: Mathematical, Physical and Chemical Tables. Springer Sciences& Business Media.

Rigaku Oxford Diffraction (2019). *CrysAlis PRO*. Rigaku Oxford Diffraction, Yarnton, England.

Scheuermann, P., Kutoglu, A., Schosnig, M., and Hoffer, E. (2000) Structure and stability of the high-pressure phase, $Ca_3TiSi_2(Al,Ti,Si)_3O_{14}$. *American Mineralogist,* **85**, 784–791.

Sokol, E., Novikov, I., Zateeva, S., Vapnik, Y., Shagam, R., and Kozmenko, O. (2010) Combustion metamorphism in the Nabi Musa dome: new implications for a mud volcanic origin of the Mottled Zone, Dead Sea area. *Basin Research*, **22**, 414–438.

Su, Y., Balmer, M.L., and Bunker, B.C. (2000) Raman spectroscopic studies of silicotitanates. *The Journal of Physical Chemistry B*, **104**, 8160–8169.

Tichý, J., Erhart, J., Kittinger, E. and Přívratská, J. (2010) Fundamentals of Piezoelectric Sensorics. Mechanical, Dielectric, and Thermodynamical Properties of Piezoelectric Materials. Chapter 7. Piezoelectric Materials. Springer-Verlag Berlin Heidelberg, 119–186.

Vapnik, Ye., Sharygin, V.V., Sokol, E.V., and Shagam, R. (2007) Paralavas in a combustion metamorphic complex: Hatrurim Basin, Israel. *Reviews in Engineering Geology*, **18**, 1–21.

Vásquez, G.C., Maestre, D., Cremades, A., and Piqueras, J. (2017) Assessment of the Cr doping and size effects on the Raman-active modes of rutile TiO_2 by UV/Visible polarized Raman spectroscopy. *Journal of Raman Spectroscopy*, **48**, 847–854.

Warr, L.N. (2021). IMA–CNMNC approved mineral symbols. *Mineralogical Magazine*, **85**(3), 291–320.Williams, S.A. (1978) Khinite, parakhinite, and dugganite three new tellurates from Tombstone, Arizona. *American Mineralogist*, **63**, 1016–10l9.

Williams, S.A. (1978) Khinite, parakhinite, and dugganite three new tellurates from Tombstone, Arizona. *American Mineralogist*, 63, 1016-10l9.

Table 1. Chemical data (in wt. %) for qeltite.

	grain used for SC-XRD			other grains in this sample		
	mean 9	range	S.D.	mean 16	range	S.D.
MgO	n.d.			0.02	0-0.07	0.02
CaO	28.27	27.94-28.75	0.25	28.19	27.63-29.04	0.42
MnO	0.16	0.10-0.21	0.04	0.084	0.01-0.18	0.04
SrO	0.37	0.30-0.40	0.03	0.30	0.23-0.39	0.05
BaO	n.d.			0.15	0-0.34	0.11
Fe_2O_3	21.62	21.08-22.12	0.30	20.71	19.14-21.80	0.79
Al_2O_3	3.78	3.49-4.12	0.23	3.98	3.31-4.74	0.46
Cr_2O_3	0.13	0.05-0.18	0.04	0.39	0.18-0.84	0.18
SiO_2	26.45	25.73-27.84	0.70	26.48	23.10-29.79	2.25
TiO_2	18.72	17.54-19.37	0.55	18.07	14.18-21.57	2.47
ZrO_2	n.d.			0.24	0.05-0.36	0.09
P_2O_5	0.11	0.05-0.17	0.04	0.22	0.13-0.50	0.10
Total	99.59			98.83		
	Calculated on 14O					
Ca	2.96			2.96		
Mn^{2+}	0.01			0.01		
Sr	0.02			0.02		
Ba				0.01		
A	***2.99***			**3**		
Ti^{4+}	0.99			0.96		
Cr^{3+}	0.01			0.03		
Zr				0.01		
B	***1***			***1***		
Si	1.99			1.98		
P^{5+}	0.01			0.02		
C	***2***			***2***		
Fe^{3+}	1.59			1.53		
Al	0.43			0.46		
Si	0.60			0.63		
Ti^{4+}	0.39			0.38		
D	***3.01***			***3.00***		

n.d. - not detected; S.D. – standard deviation

Table 2. The crystal information and details of X-ray diffraction data collection and refinement for qeltite.

Crystal data	
Structural formula	$Ca_{3.00}Ti_{1.00}Fe_{1.75}Si^*_{3.25}O_{14}$
Crystal dimensions (mm)	0.04 × 0.02 × 0.01
Crystal system, space group	Trigonal, *P*321
Temperature (K)	295.5(4)
a, b, c (Å)	8.0077(5), 8.0077(5), 4.9956(4)
$\alpha\ \beta\ \gamma$ (°)	90, 90,120
V (Å^3)	277.42(4)
Z	1
Calculated density (g cm^{-3})	3.479
μ (mm^{-1})	2.433
Data collection	
Instrument	4-circle Supernova, CCD EOS (Agilent)
Radiation type, wavelength (Å)	Ag*Kα*, 0.56087
Number of frames	748
θ range (°)	2.3176, 22.1203
Absorption correction	Multi-scan (Rigaku Oxford Diffraction, 2019)
T_{min}, T_{max}	0.83838, 0.83643
No. of measured and independent and reflections	3825, 460
R_{int}	0.0561
Data completeness to 19.69° θ (%)	100
Indices range of *h*, *k*, *l*	$-10 \le h \le 10$, $-10 \le k \le 10$, $-6 \le l \le 6$
Refinement details	
Refinement	Full-matrix least squares on F^2
Number of reflections, parameters, restraints	460/38/0
R_1 [$I > 2\sigma(I)$], R_1(all)	0.0342, 0.0622
wR_2 [$I > 2\sigma(I)$], wR_2(all)	0.0382, 0.0631
GoF	1.235
$\Delta\rho_{max}$, $\Delta\rho_{min}$ (e$^-$ Å^{-3})	0.55, −0.70
Flack parameter Determined using 153 quotients [(I+)-(I-)]/[(I+)+(I-)] (Flack, 1983; Parson *et al.*, 2013)	-0.07(5)

* - including Al

Table 3. Atomic coordinates and isotropic displacement parameters (Å^2) for qeltite.

Site	Atom	sof	*x*/a	*y*/*b*	*z*/*c*	U_{eq}
Ca*A*	Ca	1	0.5745(2)	0	0	0.0159(5)
Ti*B*	Ti	1	1	0	0	0.0125(6)
Fe*C*	Fe	0.584(12)	0	0.23812(19)	0.5	0.0121(5)
Si*C*	Si	0.416(12)	0	0.23812(19)	0.5	0.0121(5)
Si*D*	Si	1	0.3333	0.6667	0.4550(6)	0.0103(6)
O1	O	1	0.1549(6)	0.4729(6)	0.3206(8)	0.0149(10)
O2	O	1	0.3333	0.6667	0.7721(15)	0.0171(16)
O3	O	1	0.8560(8)	0.0735(8)	0.2421(10)	0.0315(14)

Table 4. Anisotropic displacement parameters (Å^2).

Site	U^{11}	U^{22}	U^{33}	U^{12}	U^{13}	U^{23}
Ca*A*	0.0150(7)	0.0218(12)	0.0133(9)	0.0109(6)	0.0014(4)	0.0028(8)
Ti*B*	0.0138(9)	0.0138(9)	0.0099(14)	0.0069(4)	0	0
Fe*C*	0.0123(9)	0.0128(7)	0.0111(8)	0.0062(4)	-0.0035(6)	-0.0018(3)
Si*C*	0.0123(9)	0.0128(7)	0.0111(8)	0.0062(4)	-0.0035(6)	-0.0018(3)
Si*D*	0.0105(9)	0.0105(9)	0.0100(14)	0.0052(4)	0	0
O1	0.016(2)	0.011(2)	0.012(2)	0.0024(19)	-0.0044(17)	0.0012(18)
O2	0.020(3)	0.020(3)	0.011(4)	0.0100(13)	0	0
O3	0.018(3)	0.041(3)	0.037(3)	0.017(3)	-0.003(2)	-0.020(2)

Table 5. Selected interatomic distances (Å) for qeltite.

atom-	atom	distance
^{A}Ca	O1	2.403(4) ×2
	O1	2.868(4) ×2
	O2	2.645(3) ×2
	O3	2.358(5) ×2
	mean	2.569
^{B}Ti	O3	1.954(5) ×6
^{C}Fe	O1	1.883(4) ×2
	O3	1.791(5) ×2
	mean	1.837
	O3	2.564(6) ×2
	mean	2.079
^{D}Si	O1	1.638(4) ×3
	O2	1.584(8)
	mean	1.62

Table 6. Bond-valence calculations for qeltite (valence units). Bond valence parameters were taken from (Gagné and Hawthorne 2015)

	O1	O2	O3	Sum
^{A}Ca	$0.2974^{2\rightarrow\downarrow}$	$0.1646^{2\rightarrow3\downarrow}$	$0.3320^{2\rightarrow\downarrow}$	1.78
	$0.0954^{2\rightarrow\downarrow}$			
^{B}Ti			$0.6739^{6\rightarrow\downarrow}$	4.04
^{C}($Fe_{0.53}Si_{0.20}Al_{0.15}Ti_{0.13}$)	$0.7225^{2\rightarrow\downarrow}$		$0.9329^{2\rightarrow\downarrow}$	3.29
			$0.1090^{2\rightarrow\downarrow}$	
^{D}Si	$0.9647^{3\rightarrow\downarrow}$	$1.1083^{\rightarrow\downarrow}$		4.00
Sum	2.08	1.60	2.05	